LETTERS
https://doi.org/10.1038/s41565-020-0728-z
nature nanotechnology

Broken mirror symmetry in excitonic response of reconstructed domains in twisted $MoSe_2/MoSe_2$ bilayers

Jiho Sung[1,2], You Zhou[1,2], Giovanni Scuri[2], Viktor Zólyomi[3,4], Trond I. Andersen[2], Hyobin Yoo[2,5], Dominik S. Wild[2], Andrew Y. Joe[2], Ryan J. Gelly[2], Hoseok Heo[1,2], Samuel J. Magorrian[3], Damien Bérubé[6], Andrés M. Mier Valdivia[7], Takashi Taniguchi[8], Kenji Watanabe[8], Mikhail D. Lukin[2], Philip Kim[2,7], Vladimir I. Fal'ko[3,9] ✉ and Hongkun Park[1,2] ✉

Van der Waals heterostructures obtained via stacking and twisting have been used to create moiré superlattices[1], enabling new optical and electronic properties in solid-state systems. Moiré lattices in twisted bilayers of transition metal dichalcogenides (TMDs) result in exciton trapping[2–5], host Mott insulating and superconducting states[6] and act as unique Hubbard systems[7–9] whose correlated electronic states can be detected and manipulated optically. Structurally, these twisted heterostructures feature atomic reconstruction and domain formation[10–14]. However, due to the nanoscale size of moiré domains, the effects of atomic reconstruction on the electronic and excitonic properties have not been systematically investigated. Here we use near-0°-twist-angle $MoSe_2/MoSe_2$ bilayers with large rhombohedral AB/BA domains[15] to directly probe the excitonic properties of individual domains with far-field optics. We show that this system features broken mirror/inversion symmetry, with the AB and BA domains supporting interlayer excitons with out-of-plane electric dipole moments in opposite directions. The dipole orientation of ground-state Γ–K interlayer excitons can be flipped with electric fields, while higher-energy K–K interlayer excitons undergo field-asymmetric hybridization with intralayer K–K excitons. Our study reveals the impact of crystal symmetry on TMD excitons and points to new avenues for realizing topologically non-trivial systems[16,17], exotic metasurfaces[18], collective excitonic phases[19] and quantum emitter arrays[20,21] via domain-pattern engineering.

To date, most studies of twisted transition metal dichalcogenide (TMD) bilayers have assumed a rigid rotation of layers without atomic-scale rearrangement[2–5]. However, recent theoretical[10] and experimental[11–14] studies have amply demonstrated that, even in these van der Waals heterostructures, the interlayer interactions can cause substantial lattice reconstruction and the resultant domain formation. Understanding how these local atomic rearrangements impact the electronic and excitonic properties of TMD heterostructures is crucial to harnessing the full potential of the so-called moiré engineering.

Here we study the spatially resolved spectroscopic properties of distinct TMD bilayer domains using twisted $MoSe_2$ homobilayers (t-$MoSe_2/MoSe_2$) as a model system. We fabricate devices incorporating t-$MoSe_2/MoSe_2$ encapsulated by hexagonal boron nitride (hBN) using the 'tear and stack' technique[1]. Figure 1a shows a dark-field transmission electron microscopy (TEM) image of a near-0°-twist-angle t-$MoSe_2/MoSe_2$ device (D1), showing black and grey regions that correspond to alternating domains with rhombohedral stacking symmetry[15] (structures schematically shown in Fig. 1b). This domain formation is caused by the rearrangement of atoms within each TMD layer to preserve interlayer commensurability, similar to observations in twisted bilayer graphene[22] and graphene on hBN[23]. Interestingly, for near-0° target twist angle, the regime we call a 'marginal twist', we observe irregular, micrometre-sized AB ($Mo_{top}Se_{bottom}$) and BA ($Se_{top}Mo_{bottom}$) domains that are large enough to be imaged optically. The irregularity of these domains probably reflects locally varying twist angles caused by strain inhomogeneity.

For t-$MoSe_2/MoSe_2$ devices used for optoelectronic characterizations, we include top and bottom graphene gates to independently control the out-of-plane electric field (E_z) and electrostatic doping (Fig. 1c)[24,25]. Figure 1d shows an integrated photoluminescence (PL) intensity map from device D2 under 1.88 eV (660 nm) excitation at 4 K. Compared with the bright, momentum-direct intralayer exciton emission from monolayer regions[26,27], the PL intensity of the twisted bilayer is reduced by three orders of magnitude, suggesting a direct-to-indirect bandgap transition from a monolayer to a bilayer. We note that the PL linewidth of the twisted bilayer is broad compared with that of a monolayer. This broadening is probably due to the additional relaxation pathway to the low-energy interlayer excitons arising from the indirect bandgap[28,29]. The PL spectra of the twisted bilayer exhibit high-energy peaks near 1.6 eV, which we label as X_0, and low-energy peaks around 1.4 eV, denoted as $X_{I,1}$ (Fig. 1e, and Supplementary Figs. 1 and 2 for the discussion of the multiple peaks). Similar to the case of other TMD bilayers[24,30,31], we assign the X_0 peaks to momentum-direct intralayer excitons composed of an electron and a hole residing in the same layer and the

[1]Department of Chemistry and Chemical Biology, Harvard University, Cambridge, MA, USA. [2]Department of Physics, Harvard University, Cambridge, MA, USA. [3]National Graphene Institute, University of Manchester, Manchester, UK. [4]Hartree Centre, STFC Daresbury Laboratory, Daresbury, UK. [5]Department of Physics, Sogang University, Seoul, Republic of Korea. [6]Department of Physics, California Institute of Technology, Pasadena, CA, USA. [7]John A. Paulson School of Engineering and Applied Sciences, Harvard University, Cambridge, MA, USA. [8]National Institute for Materials Science, Tsukuba, Japan. [9]Henry Royce Institute for Advanced Materials, University of Manchester, Manchester, UK. ✉e-mail: Vladimir.Falko@manchester.ac.uk; Hongkun_Park@harvard.edu

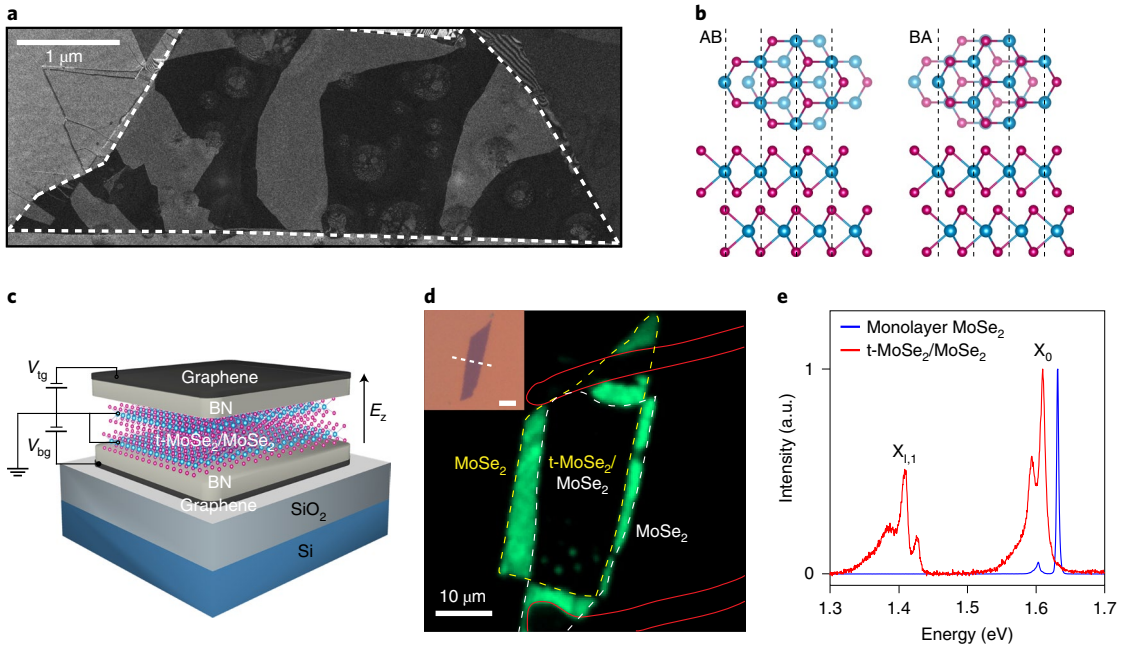

Fig. 1 | AB/BA domains in t-MoSe$_2$/MoSe$_2$ devices. a, Dark-field TEM image of D1 on a silicon nitride membrane obtained by filtering out all but one MoSe$_2$ diffraction peak ($g = 10\bar{1}0$) with the device tilted off the zone axis. The twisted bilayer region (enclosed by the dashed white line) shows alternating, micrometre-sized AB and BA domains. **b**, Top and side views of atomic structures in twinned rhombohedral AB ($Mo_{top}Se_{bottom}$) and BA ($Se_{top}Mo_{bottom}$) stacking configurations. **c**, Schematic of a t-MoSe$_2$/MoSe$_2$ device used for optoelectronic characterization. The out-of-plane electric field (E_z) and the doping concentration can be independently controlled by dual graphene gates. The black arrow defines the positive direction of E_z. **d**, A PL map of D2 at 4 K with 1.88 eV (660 nm) laser excitation. The monolayer region is enclosed by the yellow and white dashed lines, and the overlapped region is t-MoSe$_2$/MoSe$_2$. The solid red lines show the outline of a Pt contact to the top and bottom MoSe$_2$ monolayers. The original MoSe$_2$ monolayer was torn along the dashed line indicated in the inset to generate t-MoSe$_2$/MoSe$_2$. Inset scale bar, 10 μm. **e**, Normalized PL spectra from the t-MoSe$_2$/MoSe$_2$ (red) and monolayer MoSe$_2$ (blue) at $E_z = 0$.

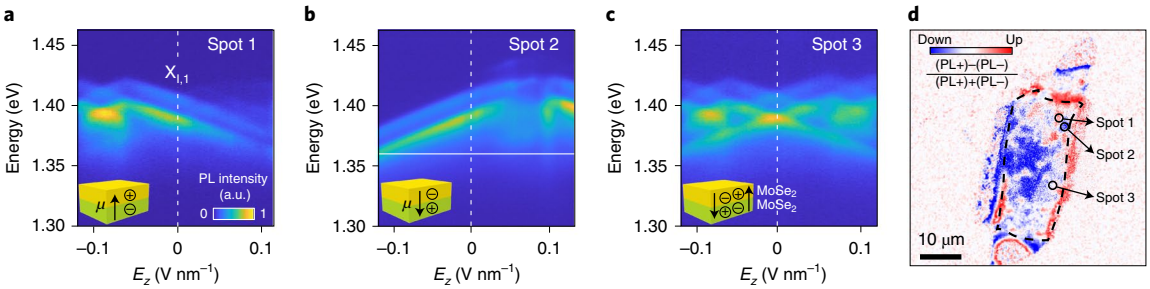

Fig. 2 | Electric-field-dependent PL spectra of the X$_{I,1}$ peaks obtained from D2 at 4 K. a–c, PL spectra of the X$_{I,1}$ peaks as a function of the electric field at spot 1 (**a**), 2 (**b**), and 3 (**c**). Inset: schematic of t-MoSe$_2$/MoSe$_2$, showing interlayer excitons with the preferred dipole moment (μ) orientation. White dotted lines, $E_z = 0$ V nm^{-1}. **d**, A map of η, defined as ((PL+) − (PL−))/((PL+) + (PL−)). PL± is the PL intensity at $E_z = \pm 0.15$ V nm^{-1}, integrated over the energy range below 1.36 eV (white solid line in **b**). Red, preferred dipole orientation up; blue, preferred dipole orientation down. The t-MoSe$_2$/MoSe$_2$ region is indicated by the dashed black line. Black solid circles represent spots 1, 2 and 3 where the spectra are taken.

X$_{I,1}$ peaks to momentum-indirect interlayer excitons in which an electron and a hole are in separate layers (see below).

Figure 2a shows PL spectra of the X$_{I,1}$ peaks as a function of E_z collected from spot 1 in device D2. The X$_{I,1}$ peaks shift linearly with E_z by as much as 50 meV, indicating that the interlayer excitons responsible for them possess a finite electric dipole moment in the out-of-plane direction. From the slope of the field-dependent energy shift, we can obtain the electron–hole distance in the X$_{I,1}$-interlayer exciton using the formula $\Delta E = -edE_z$. Here E is the energy of emission, e is the elementary charge, and d is the distance between the electron and the hole. The value of d extracted from the data in Fig. 2a is 0.26 nm, which is smaller than the interlayer distance of ~0.6 nm (ref. [30]) (Supplementary Fig. 1). Interestingly, when E_z falls below –0.09 V nm^{-1}, the slope of the linear Stark effect abruptly changes sign, indicating that the dipole moment direction changes at that field.

Importantly, at $E_z = 0$, the sign (but not the magnitude) of the Stark shift varies from spot to spot: for instance, the X$_{I,1}$ peaks at spot 2 in D2 exhibit Stark shifts with an opposite slope from those at spot 1 (Fig. 2a,b). Spot 3, on the other hand, exhibits Stark shifts with both positive and negative slopes (Fig. 2c). These observations indicate that, while the dipole-moment magnitude of the X$_{I,1}$-interlayer exciton is constant everywhere, its direction flips from spot to spot across the device, with the negative (positive) Stark slope signifying

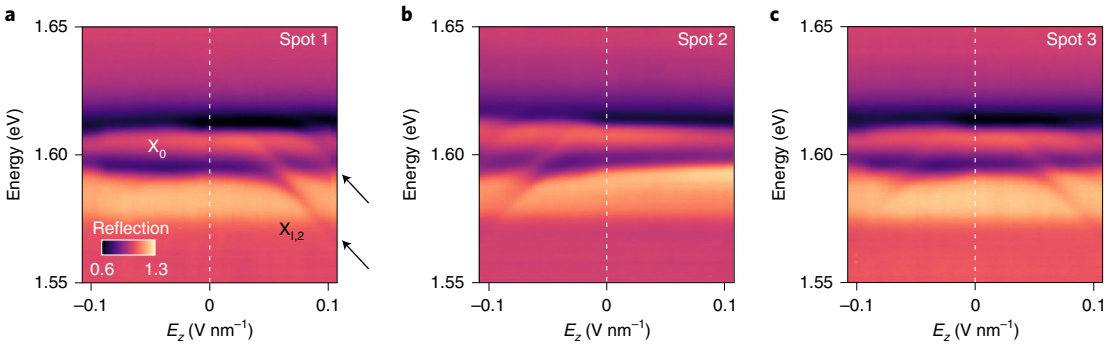

Fig. 3 | Electric-field-dependent reflectance spectra of the X_0 peaks obtained from D2 at 4 K. a–c, Reflectance spectra as a function of the electric field at spot 1 (**a**), 2 (**b**) and 3 (**c**) indicated in Fig. 2d. White dotted lines, $E_z = 0$ V nm^{-1}. The X_0 excitons exhibit avoided crossings with $X_{I,2}$ excitons (indicated by the black arrows) at positive (**a**), negative (**b**) and both (**c**) polarities of E_z. We normalize the reflected intensity using the measured reflection in the same spot in the highly electron-doped regime.

the dipole moment pointing up (down). Such behaviour is unique to near-0° t-$MoSe_2$/$MoSe_2$ devices: for instance, in $MoSe_2$ devices that incorporate a natural (untwisted) 2H bilayer (Supplementary Fig. 2), we observe the same Stark shifts at all locations.

To generate a map of the $X_{I,1}$ dipole orientation across D2, we measure the integrated PL intensity below 1.36 eV at $E_z = \pm 0.15$ V nm^{-1} (designated as PL+ and PL−, respectively) and calculate the ratio $\eta = \frac{(PL+)-(PL-)}{(PL+)+(PL-)}$: a positive (negative) η value indicates that the preferred dipole orientation is up (down). The η map in Fig. 2d clearly shows spatial domains of up (red) and down (blue) $X_{I,1}$ dipole orientations. In locations noted as white, Stark shifts of both positive and negative slopes appear, probably because the domain sizes are smaller than the probe beam size (~500 nm) and we are collecting PL spectra from both AB/BA domains.

Figure 3a–c shows reflectance spectra of the X_0 peaks (~1.6 eV) as a function of E_z at spots 1–3 in D2 indicated in Fig. 2d. The energies of the two main resonances at 1.594 eV and 1.610 eV do not vary for small E_z, indicating that the X_0 peaks originate from intralayer excitons with essentially zero out-of-plane electric dipole moment[25]. At large $|E_z|$, however, the X_0 exciton peaks exhibit avoided crossings with a new spectral feature $X_{I,2}$, which exhibits a large Stark shift (black arrows in Fig. 3a)[9]. The observed slope from the avoided crossing indicates an electric dipole moment value that corresponds to an electron–hole separation of 0.63 nm (Fig. 3a–c).

Similar to the behaviour of the $X_{I,1}$ peaks observed in Fig. 2a–c, the field-dependent avoided crossings between the X_0 and $X_{I,2}$ peaks also exhibit spatial variation across the device. As shown in Fig. 3, the avoided crossing for the lower X_0 peak occurs at $E_z = 0.07$ V nm^{-1} at spot 1 (Fig. 3a), at $E_z = -0.07$ V nm^{-1} at spot 2 (Fig. 3b) and for both polarities at spot 3 (Fig. 3c). We note that the PL spectra presented in Supplementary Fig. 3 also exhibit avoided crossing behaviour, similar to those seen in Fig. 3. Specifically, the lower X_0 peak and the $X_{I,2}$ peak show a field-dependent avoided crossing near $|E_z| = 0.07$ V nm^{-1} (Supplementary Fig. 3). Importantly, the spatial map of the avoided crossing features (Supplementary Fig. 4) agrees well with the dipole orientation map in Fig. 2d, strongly suggesting a common physical origin.

The spatially dependent optical properties in Figs. 2 and 3 can be understood from the electronic band structure of AB/BA ($Mo_{top}Se_{bottom}$/$Se_{top}Mo_{bottom}$) domains in t-$MoSe_2$/$MoSe_2$. Unlike natural 2H $MoSe_2$ bilayers, the crystal structures of the AB (BA) domains are not mirror/inversion symmetric: in particular, because the top and bottom layers are clearly distinguished by the crystal structure, electrons and holes can preferentially reside in the top or bottom layers, leading to interlayer excitons with preferred dipole orientation.

The broken mirror symmetry of the AB ($Mo_{top}Se_{bottom}$) domain is reflected in the properties of the states at its band edges. Density functional theory (DFT) calculations of the AB-stacked $MoSe_2$/$MoSe_2$ bilayer show that the valence band maximum (VBM) is at the Γ point, and the conduction band minimum (CBM) can be at the Q or K point depending on the calculation parameters (Fig. 4a and Supplementary Fig. 5). While the hole wavefunction at the Γ point is equally distributed over both layers, the electron wavefunction is more localized in the top layer (as compared with the bottom) regardless of whether the CBM is at the Q or K point (Fig. 4b and Table 2). We note that this asymmetry is much stronger for the K-point band extremum (100%) than for the Q point (~60%). These results indicate that electrons prefer to reside in the top layer in AB-stacked $MoSe_2$/$MoSe_2$, and consequently the momentum-indirect interlayer excitons responsible for the $X_{I,1}$ peaks should have a downward dipole orientation. Because BA stacking is just a mirror image of AB stacking with respect to the horizontal plane, the preferred dipole orientation of the $X_{I,1}$-interlayer exciton is upwards in BA domains.

Quantitative comparisons between experimental data and DFT calculations provide further insight into the nature of the $X_{I,1}$-interlayer excitons. The DFT calculations show that the electron–hole separations for Γ–K and Γ–Q interlayer excitons are 0.34 nm and 0.07 nm, respectively (Table 1). Experimentally, the electron–hole separation deduced from the $X_{I,1}$-peak Stark shifts (Fig. 2a–c) is 0.26 nm. Comparison of the dipole-moment values suggests that the $X_{I,1}$-interlayer excitons are probably from the Γ–K transition in AB/BA domains of t-$MoSe_2$/$MoSe_2$ (ref. [31]). The field-dependent flip of the dipole orientation observed in Fig. 2a,b provides further support for this assignment: by extrapolating the line with a negative slope at spot 2 to $E_z = 0$, we find a zero-field splitting of 43 meV between the two dipole orientations, which agrees well with DFT calculations for the two Γ–K transitions (the energy separations between two Γ–Q transitions should be orders of magnitude larger; Supplementary Fig. 6).

The avoided crossing behaviour between the X_0 and $X_{I,2}$ peaks in Fig. 3a–c can also be understood from DFT calculations of AB-stacked $MoSe_2$/$MoSe_2$. In AB-stacked $MoSe_2$/$MoSe_2$, the two monolayers exhibit staggered band alignment at the K (or K′) point, and the K–K intralayer excitons (X_0) in the bottom layer have a lower energy than those in the top layer (Fig. 4c): this explains the origin of the two X_0 peaks observed in Figs. 1e and 3a–c. Meanwhile, the electron and the hole from different layers can form momentum-direct, K–K interlayer excitons as shown in Fig. 4c[9,28,29,32] (see the time-resolved PL data in Supplementary Fig. 7, which show that the lifetime of the X_0–$X_{I,2}$ exciton (0.03 ns) is much shorter than that of the momentum-indirect $X_{I,1}$-interlayer exciton[33]).

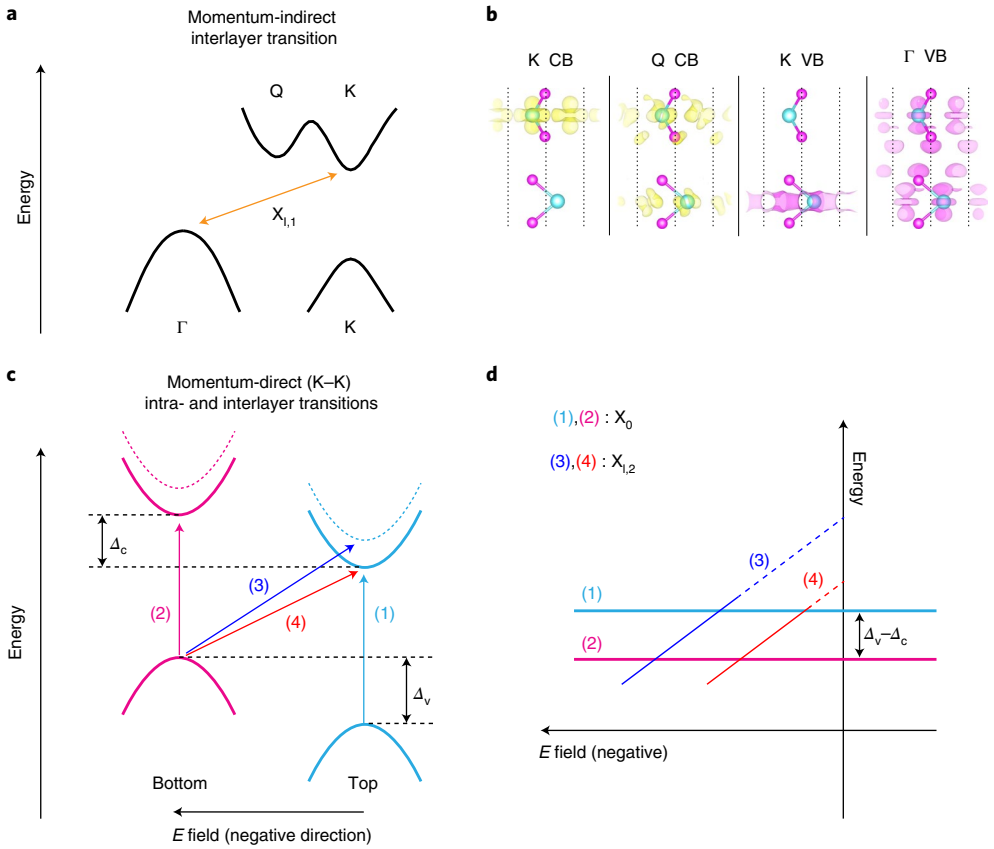

Fig. 4 | Electronic band structure of AB-stacked $MoSe_2/MoSe_2$. **a**, Electronic band structure of an AB-stacked $MoSe_2/MoSe_2$ bilayer with the VBM at the Γ point and the CBM at either the K or Q points. The data in Fig. 2 suggest that momentum-indirect interlayer excitons, $X_{I,1}$ are from the Γ–K transition (orange arrow). **b**, Contour plots of the electron wavefunctions at the conduction-band K and Q points and the hole wavefunctions at the valence-band K and Γ points. Atomic decomposition of wavefunctions at the K and Q points in the conduction band and that at the K and Γ points in the valence band is shown in Table 2. The calculated dipole moment of each state is shown in the last row of Table 2. **c**, The electronic band structure of AB-stacked $MoSe_2/MoSe_2$ at the K valley. Electronic states localized in the top (bottom) are drawn in cyan (magenta) colour, while the solid and dashed line represent spin up and down states. The optical transitions (1) and (2) correspond to momentum-direct intralayer transitions (X_0), while (3) and (4) represent the momentum-direct (K–K) interlayer transitions ($X_{I,2}$). The value of the energy splitting between the top and bottom layer K valley conduction band (Δ_c) obtained from the DFT calculations is 50 meV, and that of the valence band (Δ_v) is 62 meV at $E_z = 0$. The black arrow at the bottom represents the negative direction of an out-of-plane electric field. The energy of the interlayer transition from the bottom layer VBM to the top layer CBM (3 and 4) is reduced under negative E_z. **d**, The energy of X_0 (1 and 2 in **c**) and $X_{I,2}$ (3 and 4 in **c**) transitions as a function of E_z. Due to the reduced binding energy of $X_{I,2}$, the energy of $X_{I,2}$ at $E_z = 0$ is higher than X_0.

Table 1 | The calculated dipole moment of interlayer excitons from momentum-indirect Γ–K and Γ–Q and momentum-direct K–K transitions

Interlayer excitons	d_z (e nm)
Γ hole–K electron	0.34
Γ hole–Q electron	0.07
K hole–K electron	0.64

Table 2 | Sublattice decomposition of wavefunctions at the K and Q points in the conduction band and that at the K and Γ points in the valence band

$\|\psi\|^2$ (%)	K CB	Q CB	K VB	Γ VB
Top				
Se	3.8	6.5	0.0	1.0
Mo	92.2	42.6	0.7	31.9
Se	3.8	10	0.2	14.3
Bottom				
Se	0.0	6.8	7.5	14.9
Mo	0.1	29.7	84.0	36.6
Se	0.0	4.3	7.5	1.2
d_z (e nm)	0.322	0.058	−0.317	−0.017

These K–K interlayer excitons responsible for the $X_{I,2}$ peaks do not show any reflection contrast at $E_z = 0$ but acquire oscillator strength and cause avoided crossings when they become resonant with the X_0 intralayer excitons, as shown in Fig. 4d[9]. The avoided crossing occurs at opposite E_z in the AB and BA domains (Fig. 3a–c) because the preferred dipole orientation of the $X_{I,2}$ excitons is flipped in the two domains (see Table 1 for quantitative comparison). Moreover, because the electrons and holes of the $X_{I,2}$ excitons are largely localized in separate $MoSe_2$ layers (Fig. 4b and Table 2), the electron–hole separation should be equal to the interlayer distance (~0.6 nm), consistent with the separation extracted from the data in Fig. 3a–c. While further studies will be necessary to account for the coupling strengths between inter- and intralayer excitons[34,35], the band

structure presented in Fig. 4 provides a qualitative understanding of the main features in Figs. 2 and 3.

The domain-resolved spectroscopy of rhombohedral AB/BA domains in t-$MoSe_2$/$MoSe_2$ bilayers presented here demonstrates that local atomic registry and crystal symmetry have profound impacts on the excitonic properties of these heterostructures. Specifically, our observations indicate that the interlayer excitons in AB and BA domains exhibit opposite electric dipole orientations dictated by crystal symmetry, as manifested by the spatial dependence of the $X_{I,1}$ Stark shift and the X_0–$X_{I,2}$ avoided crossing. Our observations indicate that the domain-specific, electrically tunable, optical properties of twisted TMD bilayers can be used to realize a wide variety of exciting potential applications. These include proposed excitonic topological insulators[16,17], quantum metasurfaces[18] and strongly correlated exciton lattices for Hubbard model physics[19–21]. Importantly, a tessellation of AB/BA domains in twisted TMD homobilayers[10–14] can be used to generate alternating dipolar exciton arrays whose relative energy and coupling strengths can be engineered by changing the twist angle and out-of-plane electric field. In such systems, it should also be possible to change the exciton–exciton interactions from attractive to repulsive[36] via field-dependent dipole flipping. We also note that there have been extensive research efforts towards controlling the domain size and moiré length scales[37] as well as visualizing domains in a non-destructive way[12,13]. These techniques, together with future research, could enable the realization of spatially homogeneous arrays of excitons, thus opening the door for the realization of many exotic exciton states, such as antiferroelectric exciton droplets[38], exciton liquids[39] and exciton condensates[40].

Online content

Any methods, additional references, Nature Research reporting summaries, source data, extended data, supplementary information, acknowledgements, peer review information; details of author contributions and competing interests; and statements of data and code availability are available at https://doi.org/10.1038/s41565-020-0728-z.

Received: 3 December 2019; Accepted: 3 June 2020;
Published online: 13 July 2020

References

1. Cao, Y. et al. Unconventional superconductivity in magic-angle graphene superlattices. *Nature* **556**, 43–50 (2018).
2. Seyler, K. L. et al. Signatures of moiré-trapped valley excitons in $MoSe_2$/WSe_2 heterobilayers. *Nature* **567**, 66–70 (2019).
3. Tran, K. et al. Evidence for moiré excitons in van der Waals heterostructures. *Nature* **567**, 71–75 (2019).
4. Jin, C. et al. Observation of moiré excitons in WSe_2/WS_2 heterostructure superlattices. *Nature* **567**, 76–80 (2019).
5. Alexeev, E. M. et al. Resonantly hybridized excitons in moiré superlattices in van der Waals heterostructures. *Nature* **567**, 81–86 (2019).
6. Wang, L. et al. Correlated electronic phases in twisted bilayer transition metal dichalcogenides. *Nat. Mater.* https://doi.org/10.1038/s41563-020-0708-6 (2020).
7. Tang, Y. et al. Simulation of Hubbard model physics in WSe_2/WS_2 moiré superlattices. *Nature* **579**, 353–358 (2020).
8. Regan, E. C. et al. Mott and generalized Wigner crystal states in WSe_2/WS_2 moiré superlattices. *Nature* **579**, 359–363 (2020).
9. Shimazaki, Y. et al. Strongly correlated electrons and hybrid excitons in a moiré heterostructure. *Nature* **580**, 472–477 (2020).
10. Enaldiev, V. V., Zólyomi, V., Yelgel, C., Magorrian, S. J. & Fal'ko, V. I. Stacking domains and dislocation networks in marginally twisted bilayers of transition metal dichalcogenides. *Phys. Rev. Lett.* **124**, 206101 (2020).
11. Weston, A. et al. Atomic reconstruction in twisted bilayers of transition metal dichalcogenides. *Nat. Nanotechnol.* https://doi.org/10.1038/s41565-020-0682-9 (2020).
12. McGilly, L. J. et al. Visualization of moiré superlattices. *Nat. Nanotechnol.* https://doi.org/10.1038/s41565-020-0708-3 (2020).
13. Sushko, A. et al. High resolution imaging of reconstructed domains and moire patterns in functional van der Waals heterostructure devices. Preprint at http://arxiv.org/abs/1912.07446 (2019).
14. Rosenberger, M. R. et al. Twist angle-dependent atomic reconstruction and moiré patterns in transition metal dichalcogenide heterostructures. *ACS Nano* **14**, 4550–4558 (2020).
15. Toh, R. J., Sofer, Z., Luxa, J., Sedmidubský, D. & Pumera, M. 3R phase of MoS_2 and WS_2 outperforms the corresponding 2H phase for hydrogen evolution. *Chem. Commun.* **53**, 3054–3057 (2017).
16. Wu, F., Lovorn, T. & MacDonald, A. H. Topological exciton bands in moiré heterojunctions. *Phys. Rev. Lett.* **118**, 147401 (2017).
17. Perczel, J. et al. Topological quantum optics in two-dimensional atomic arrays. *Phys. Rev. Lett.* **119**, 023603 (2017).
18. Bekenstein, R. et al. Quantum metasurfaces with atom arrays. *Nat. Phys.* **16**, 676–681 (2020).
19. Byrnes, T., Recher, P. & Yamamoto, Y. Mott transitions of exciton polaritons and indirect excitons in a periodic potential. *Phys. Rev. B* **81**, 205312 (2010).
20. Yu, H., Liu, G.-B., Tang, J., Xu, X. & Yao, W. Moiré excitons: From programmable quantum emitter arrays to spin-orbit–coupled artificial lattices. *Sci. Adv.* **3**, e1701696 (2017).
21. Wu, F., Lovorn, T. & MacDonald, A. H. Theory of optical absorption by interlayer excitons in transition metal dichalcogenide heterobilayers. *Phys. Rev. B* **97**, 035306 (2018).
22. Yoo, H. et al. Atomic and electronic reconstruction at the van der Waals interface in twisted bilayer graphene. *Nat. Mater.* **18**, 448–453 (2019).
23. Woods, C. R. et al. Macroscopic self-reorientation of interacting two-dimensional crystals. *Nat. Commun.* **7**, 10800 (2016).
24. Wang, Z., Chiu, Y.-H., Honz, K., Mak, K. F. & Shan, J. Electrical tuning of interlayer exciton gases in WSe_2 bilayers. *Nano Lett.* **18**, 137–143 (2018).
25. Jauregui, L. A. et al. Electrical control of interlayer exciton dynamics in atomically thin heterostructures. *Science* **366**, 870–875 (2019).
26. Scuri, G. et al. Large excitonic reflectivity of monolayer $MoSe_2$ encapsulated in hexagonal boron nitride. *Phys. Rev. Lett.* **120**, 037402 (2018).
27. Zhou, Y. et al. Controlling excitons in an atomically thin membrane with a mirror. *Phys. Rev. Lett.* **124**, 027401 (2020).
28. Horng, J. et al. Observation of interlayer excitons in $MoSe_2$ single crystals. *Phys. Rev. B* **97**, 241404 (2018).
29. Gerber, I. C. et al. Interlayer excitons in bilayer MoS_2 with strong oscillator strength up to room temperature. *Phys. Rev. B* **99**, 035443 (2019).
30. Liu, K. et al. Evolution of interlayer coupling in twisted molybdenum disulfide bilayers. *Nat. Commun.* **5**, 4966 (2014).
31. Kunstmann, J. et al. Momentum-space indirect interlayer excitons in transition-metal dichalcogenide van der Waals heterostructures. *Nat. Phys.* **14**, 801–805 (2018).
32. Deilmann, T. & Thygesen, K. S. Interlayer excitons with large optical amplitudes in layered van der Waals materials. *Nano Lett.* **18**, 2984–2989 (2018).
33. Miller, B. et al. Long-lived direct and indirect interlayer excitons in van der Waals heterostructures. *Nano Lett.* **17**, 5229–5237 (2017).
34. Daniels, J. M., Machnikowski, P. & Kuhn, T. Excitons in quantum dot molecules: Coulomb coupling, spin-orbit effects, and phonon-induced line broadening. *Phys. Rev. B* **88**, 205307 (2013).
35. Ruiz-Tijerina, D. A. & Fal'ko, V. I. Interlayer hybridization and moiré superlattice minibands for electrons and excitons in heterobilayers of transition-metal dichalcogenides. *Phys. Rev. B* **99**, 125424 (2019).
36. Hubert, C. et al. Attractive dipolar coupling between stacked exciton fluids. *Phys. Rev. X* **9**, 021026 (2019).
37. Ribeiro-Palau, R. et al. Twistable electronics with dynamically rotatable heterostructures. *Science* **361**, 690–693 (2018).
38. Sammon, M. & Shklovskii, B. I. Attraction of indirect excitons in van der Waals heterostructures with three semiconducting layers. *Phys. Rev. B* **99**, 165403 (2019).
39. Stern, M., Umansky, V. & Bar-Joseph, I. Exciton liquid in coupled quantum wells. *Science* **343**, 55–57 (2014).
40. Wang, Z. et al. Evidence of high-temperature exciton condensation in two-dimensional atomic double layers. *Nature* **574**, 76–80 (2019).

Methods

Sample preparation and optical spectroscopy. Monolayer $MoSe_2$, few-layer graphene and hBN flakes were exfoliated onto silicon substrates with a 285 nm silicon oxide layer. Monolayers of $MoSe_2$ were identified under an optical microscope and verified via PL measurements. The thickness of hBN flakes was determined with atomic force microscopy. The pre-patterned platinum contact for a $MoSe_2$ monolayer was first defined with electron-beam lithography and electron-beam evaporation (1 nm chromium + 10 nm platinum) on top of the hBN/graphene heterostructure. The graphene/hBN/$MoSe_2$/$MoSe_2$ heterostructure was prepared using a dry transfer method, using the tear-and-stack technique to form twisted bilayer $MoSe_2$. This heterostructure was then transferred onto the pre-patterned platinum contacts and hBN/graphene heterostructure to form graphene/hBN/$MoSe_2$/$MoSe_2$/hBN/graphene. Next, electrical contacts to the platinum and few-layer graphene gates were defined with electron-beam lithography and deposited via thermal evaporation (10 nm chromium + 90 nm gold). Optical measurements were carried out in a home-built confocal microscope using an objective with a numerical aperture of 0.75 in a 4 K cryostat from Montana Instruments. For PL measurements, a 660-nm-wavelength diode laser was used for excitation. To obtain the reflectance spectra, we used a halogen lamp with a broad spectral range as the light source. The spatial image of the avoided crossing features was obtained using a Ti:sapphire laser from M Squared.

TEM experiment. The TEM sample was prepared by transferring D1 onto a 50-nm-thick silicon nitride membrane. Dark-field imaging was performed in an 80 kV field-emission TEM (JEOL 2010F) equipped with a Gatan OneView camera. Off-zone axis $g = 10\bar{1}0$ DF imaging exhibits AB/BA domain contrast associated with the antisymmetric shift of the lattice period in AB and BA regions[41].

DFT calculations. We used the local density approximation with spin–orbit coupling taken into account to compute the band structure of the t-$MoSe_2$/$MoSe_2$ bilayers, utilizing the VASP code[42]. We used the basis composed of plane waves with a cutoff energy of 600 eV and projector augmented wave pseudopotentials. The in-plane Brillouin zone was sampled by a 12×12 grid. The 2D systems were modelled in a periodic three-dimensional box with a vertical distance of 20 between repeated images of the bilayers. The equilibrium structural parameters were taken from experiments in the literature[43].

Time-resolved PL experiment. A SuperK supercontinuum laser with SuperK VARIA centred at 660 nm with a repetition rate of 80 MHz and an average power of 2 μW was employed, and the collected PL was detected by the time-correlated single-photon counting method with a Picoharp 300.

Data availability

The data that support the plots within this paper and other findings of this study are available from the corresponding author upon reasonable request.

References

41. Brown, L. et al. Twinning and twisting of tri- and bilayer graphene. *Nano Lett.* **12**, 1609–1615 (2012).
42. Kresse, G. & Furthmüller, J. Efficient iterative schemes for ab initio total-energy calculations using a plane-wave basis set. *Phys. Rev. B* **54**, 11169 (1996).
43. Bronsema, K. D., De Boer, J. L. & Jellinek, F. On the structure of molybdenum diselenide and disulfide. *Z. Anorg. Allg. Chem.* **540**, 15–17 (1986).

Acknowledgements

We thank B. Urbaszek for helpful discussions. We acknowledge support from the DoD Vannevar Bush Faculty Fellowship (N00014-16-1-2825 for H.P., N00014-18-1-2877 for P.K.), NSF (PHY-1506284 for H.P. and M.D.L.), NSF CUA (PHY-1125846 for H.P. and M.D.L.), AFOSR MURI (FA9550-17-1-0002), ARL (W911NF1520067 for H.P. and M.D.L.), the Gordon and Betty Moore Foundation (GBMF4543 for P.K.), ONR MURI (N00014-15-1-2761 for P.K.), and Samsung Electronics (for P.K. and H.P.). V.I.F. acknowledges EPSRC grants no. EP/S019367/1, EP/S030719/1, EP/N010345/1, ERC Synergy Grant Hetero2D, Lloyd's Register Foundation Nanotechnology Grant, European Graphene Flagship Project and European Quantum Technologies Project 2D-SIPC. The device fabrication was carried out at the Harvard Center for Nanoscale Systems. K.W. and T.T. acknowledge support from the Elemental Strategy Initiative conducted by the MEXT, Japan and the CREST (JPMJCR15F3), JST. D.B. acknowledges support from the Summer Undergraduate Research Fellowship at Caltech.

Author contributions

H.P., P.K., J.S., Y.Z., G.S., H.Y. and D.S.W. conceived the study, and J.S., Y.Z., G.S., T.I.A, A.Y.J., R.J.G., D.B. and A.M.M.V. fabricated the devices and performed the optical spectroscopy. H.P. V.I.F. J.S., Y.Z., G.S., V.Z., T.I.A. and D.S.W. analysed the data. V.I.F., V.Z. and S.J.M. performed the DFT calculations. H.Y. performed electron microscopy measurements. H.H. performed $MoSe_2$ crystal growth. T.T. and K.W. performed h-BN crystal growth. J.S., Y.Z., G.S., T.I.A, M.D.L., P.K., V.I.F. and H.P. wrote the manuscript with extensive input from all authors. H.P., V.I.F., P.K. and M.D.L. supervised the project.

Competing interests

The authors declare no competing interests.

Additional information

Supplementary information is available for this paper at https://doi.org/10.1038/s41565-020-0728-z.

Correspondence and requests for materials should be addressed to V.I.F. or H.P.

Reprints and permissions information is available at www.nature.com/reprints.